UC Irvine
UC Irvine Electronic Theses and Dissertations

Title
Characterization of Magnetic Tunnel Junctions For Spin Transfer Torque Magnetic Random Access Memory

Permalink
https://escholarship.org/uc/item/4c03d1rm

Author
Dill, Joshua

Publication Date
2014

Copyright Information
This work is made available under the terms of a Creative Commons Attribution License, availalbe at https://creativecommons.org/licenses/by/4.0/

Peer reviewed|Thesis/dissertation

eScholarship.org Powered by the California Digital Library
University of California

UNIVERSITY OF CALIFORNIA,
IRVINE

Characterization of Magnetic Tunnel Junctions For Spin Transfer Torque Magnetic Random Access Memory

THESIS

submitted in partial satisfaction of the requirements
for the degree of

MASTER OF SCIENCE

in Chemical and Materials Physics - Physics

by

Joshua Luchay Dill

Thesis Committee:
Professor Ilya N. Krivorotov, Chair
Professor Philip G. Collins
Professor Michael Dennin

2014

© 2014 Joshua Luchay Dill

DEDICATION

To My Parents, Bill and Linda

TABLE OF CONTENTS

Page

LIST OF FIGURES **iv**

ACKNOWLEDGMENTS **v**

ABSTRACT OF THE THESIS **vi**

1 Introduction **1**

2 Background **3**
- 2.1 Magnetic Tunnel Junctions . . . 3
- 2.2 Tunneling Magnetoresistance . . . 5
- 2.3 Spin-Transfer Torque . . . 8
- 2.4 Spin-Transfer Torque Driven Magnetization Dynamics and Switching . . . 10

3 Experimental Procedures **14**
- 3.1 Field Modulated Spin-Torque-Driven Ferromagnetic Resonance . . . 15
- 3.2 Write Error Rates . . . 25

4 Results **33**

5 Conclusions **40**

Bibliography **41**

Appendix **44**
- A Write Error Rate Code . . . 44
- B Phase Adjustment Code . . . 47

LIST OF FIGURES

Page

2.1 Magnetic Tunnel Junction States 4
2.2 Tunneling Magnetoresistance Diagram 6
2.3 Resistance vs Field For MTJs 7
2.4 Energy Versus Magnetization Angle 8
2.5 Spin-Transfer Torque Simplified Illustration 9
2.6 Magnetic Precession and Torques 12
2.7 Spin-Transfer Torque Driven Precession 13

3.1 Comparison of ST-FMR Spectra 21
3.2 FM ST-FMR Circuit 22
3.3 Write Error Rate Pulse Train 26
3.4 Write Error Rate Circuit 29

4.1 MTJ Layer Structure 34
4.2 Fe-rich Resistance Versus Applied Field 35
4.3 Co-rich Resistance Versus Applied Field 35
4.4 Fe-rich Versus Co-rich WER 36
4.5 Fe-rich WER Versus Applied Field 38
4.6 Fe-rich FM ST-FMR Spectra 39
4.7 Co-rich FM ST-FMR Spectra 39

ACKNOWLEDGMENTS

First, I would like to thank my friends and family whose involvement in my life has been instrumental to my happiness and successes so far.

I would like to thank my lab mates, past and present, for their useful advice, enlightening conversations, and helpful insights.

I would of course like to thank my research advisor Professor Ilya Krivorotov, whose guidance allowed me to grow into a better scientist and whose vast knowledge of the field provided insights into even the most unclear situations.

I would also like to thank the other members of my committee, Professors Philip Collins and Michael Dennin both for their time and effort in the review of my thesis.

ABSTRACT OF THE THESIS

Characterization of Magnetic Tunnel Junctions For
Spin Transfer Torque Magnetic Random Access Memory

By

Joshua Luchay Dill

Master of Science in Chemical and Materials Physics - Physics

University of California, Irvine, 2014

Professor Ilya N. Krivorotov, Chair

This thesis details two experimental methods for quantifying magnetic tunnel junction behavior, namely write error rates and field modulated spin-torque ferromagnetic resonance. The former examines how reliably an applied spin-transfer torque can excite magnetization dynamics that lead to a reversal of magnetization direction while the latter studies steady state dynamics provided by an oscillating spin-transfer torque. These characterization techniques reveal write error rate behavior for a particular composition magnetic tunnel junction that qualitatively deviates from theoretical predictions. Possible origins of this phenomenon are also investigated with the field modulated spin-torque ferromagnetic resonance technique. By understanding the dynamics of magnetic moments predicted by theory, one can experimentally confirm or disprove these theories in order to accurately model and predict tunnel junction behavior. By having a better model for what factors are important in magnetization dynamics, one can optimize these factors in terms of improving magnetic tunnel junctions for their use as computer memory.

Chapter 1

Introduction

Traditionally the manipulation of electron charge, or electronics, has been the basis of computer technology. However more recently, advances have been made using electron spin (in the form of spin-polarized current) to control a material's magnetization, hence named spintronics. When the spins of electrons in a material are aligned in a uniform direction (a ferromagnet), the spin of an electron current passing through the material interacts with the aligned spins in such a way that can be detected and controlled electrically. This behavior can be exploited to store and manipulate information, commercialized first by magnetic hard-disk drives. Based in traditional electronics, current market standard dynamic random-access memory (DRAM) uses a charged or discharged capacitor to represent the two values of a bit, "0" & "1". This type of memory is known as volatile because the capacitor dissipates charge through an attached transistor over time, requiring a periodic recharging when in operation, and will therefore lose the stored information after power is turned off. Within the past decade, research has ignited in the development of magnetic RAM, with a front-runner being spin-transfer torque magnetic random access memory (STT-MRAM). STT-MRAM, like all magnetic memory, is non-volatile because the information is stored in the magnetization of nano-scale magnetic structures and does not need power to retain its state. Without

the need for continual refresh energy consumption, STT-MRAM offers a significantly smaller power consumption, as well as improved scalability and speed compared to current memories in the market [1]. This new technology has just begun to enter the commercial market but can be found in the R&D department of most major computer technology companies today.

This thesis examines experimental methods used to characterize STT-MRAM in order to better understand and refine the technology. Chapter 2 explains STT-MRAM devices and the physics which governs their behavior. Chapter 3 describes and contextualizes the experimental procedures that constitute the characterization methods. Chapter 4 discusses the results (and their implications) attained from the procedures in the the previous chapter on two variations of memory cells for possible use in STT-MRAM. Lastly, concluding remarks are offered in Chapter 5.

Chapter 2

Background

This chapter will introduce a new form of computer memory and describe the underlying physics which governs its behavior.

2.1 Magnetic Tunnel Junctions

Magnetic tunnel junctions (MTJs) are magnetic heterostructures with three main functional components: a fixed ferromagnetic layer (or reference layer), an insulating tunnel barrier (the current standard being crystalline MgO), and a free ferromagnetic layer (or storage layer). The fixed layer is usually pinned in place by either being more voluminous than the free layer or coupling to a nearby synthetic antiferromagnetic (SAF, or pinning layer). Each of these magnetic layers (often made of CoFeB) can be viewed as a single magnetic moment, known as the macrospin approximation, oriented in a particular direction. Most MTJs are fabricated in such a way as to have two stable magnetic orientations, usually along the same axis but in opposite directions. This can be achieved by patterning the stack into something such as an elliptical nanopillar whose shape creates two energy minima for the magnetic

moments along the long axis of the ellipse. The magnetic layers can then arrange themselves into two orientations relative to one another, parallel (or P state) and antiparallel (or AP state). These two states (visualized in Fig. 2.1) serve as the 1's and 0's for STT-MRAM. There are multiple configurations to this basic MTJ design developed throughout ongoing research in the field [1], however this thesis will only focus on MTJs with a free and fixed layer with both magnetizations aligned in the plane of the layers (so-called in-plane MTJs).

In order to serve as practical computer memory, a device needs to have two core properties: readability, being able to read off the current state of the device, and writability, being able to flip the current state of the device. These necessary properties for an MTJ to function as magnetic memory are facilitated by two quantum mechanical effects present in MTJs: tunneling magnetoresistance and spin-transfer torque. Tunneling magnetoresistance (covered in section 2.2) causes the two magnetic states to have different electrical resistances, allowing for a simple method to measure the current state of the MTJ. Spin-transfer torque (covered in sections 2.3 & 2.4) excites precessional dynamics of the free layer magnetization by passing a current through the MTJ. When the current reaches a critical value, it can incite a precession large enough to reverse the direction of the free layer. This effect fulfills the second criterion of writability. By meeting these two criteria, as well as being non-volatile and having predicted high scalability and speed, MTJs used in STT-MRAM stand out as a promising next-generation memory.

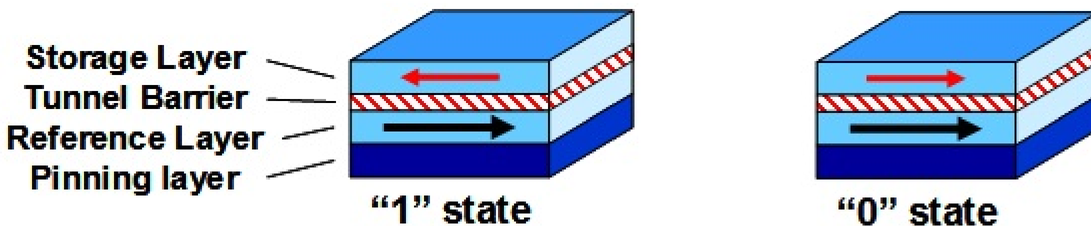

Figure 2.1: The two resistance states of a MTJ, parallel (right) and antiparallel (left). From Azom.com.

2.2 Tunneling Magnetoresistance

A classical physics view of electron transport would not allow for a current to flow across an insulating barrier, as it would mean electrons would have to pass through a classically "forbidden" region. But with a quantum mechanical interpretation, an electron wave function is known to penetrate and exponentially decay into an insulator, allowing for tunneling transport if the barrier is sufficiently thin. First predicted by Jullière [2] under the assumption that electron spin is conserved across the barrier, this tunneling current will depend upon the relative density of states of the two ferromagnetic layers. Based on Fermi's Golden Rule, Jullière's model of tunneling magnetoresistance (TMR) states the conductance of each magnetic configuration (G_P & G_{AP}) is proportional to the density of states as follows:

$$G_P \propto \rho_{1\uparrow}\rho_{2\uparrow} + \rho_{1\downarrow}\rho_{2\downarrow} \tag{2.1}$$

$$G_{AP} \propto \rho_{1\uparrow}\rho_{2\downarrow} + \rho_{1\downarrow}\rho_{2\uparrow} \tag{2.2}$$

where $\rho_{1\uparrow}$ and $\rho_{1\downarrow}$ ($\rho_{2\uparrow}$ and $\rho_{2\downarrow}$) are the density of states at the Fermi energy of the majority and minority spins of the first (second) ferromagnetic layer. This can be viewed as a two current model, one for each spin state, depicted by Fig. 2.2. In this model, the current whose spin is the majority spin of both ferromagnetic layers will dominate over currents of minority spins or mixed majority and minor spins. This results in a lower resistance P state (because current can flow more easily) and higher resistance AP state. Now, if one defines spin polarization P_i for the i-th ferromagnetic layer as the net spin for electronic states at the Fermi surface:

$$P_i = \frac{\rho_{i\uparrow} - \rho_{i\downarrow}}{\rho_{i\uparrow} + \rho_{i\downarrow}} \tag{2.3}$$

the TMR ratio can be defined as the relative change in resistance and calculated in terms of the spin polarization:

$$TMR \equiv \frac{R_{AP} - R_P}{R_P} = \frac{G_P - G_{AP}}{G_{AP}} = \frac{2P_1P_2}{1 + P_1P_2} \tag{2.4}$$

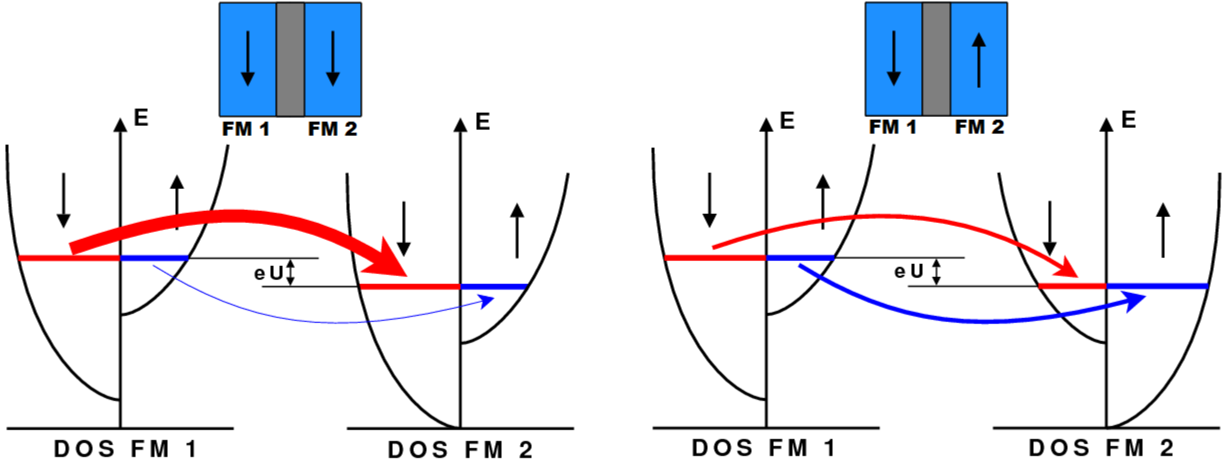

Figure 2.2: A depiction of Jullière's tunneling magnetoresistance, in which the parallel configuration of the ferromagnetic layers (left) results in a larger conductance than the antiparallel configuration (right). The arrows indicate conductance across the barrier for each spin current, where a thicker arrow denotes a larger conductance, and eU is the energy difference across the barrier. From Wikimedia Commons.

A more detailed approach to TMR was taken by Butler [3], which was very applicable to the MgO-based MTJ that has become ubiquitous throughout its field of research. Butler analyzed epitaxial interfaces such as Fe|MgO|Fe with the Bloch states of the electrons near the Fermi surface. The bulk band structure reveals three primary evanescent tunneling states, where the mode that decays the slowest through the barrier (and therefore dominates the conductance) is only accessible to spin majority electrons at the Fermi level. This causes the lattice-matched tunnel barrier to act as an additional spin polarizer and filter for the current passing through a MTJ. Using this model, TMR ratios can theoretically reach over 1000%. In practice, TMR ratios over 600% have so far been realized at room temperature for crystalline MgO-based MTJs [4]. TMR's dependence as a function of angle θ between the magnetizations of the two ferromagnetic layers in MTJ-like structures is still not wholly

understood. However, the conductance G is given to good approximation by [5]:

$$G(\theta) = \frac{G_P - G_{AP}}{2}(1 + P_1 P_2 \cos\theta) \tag{2.5}$$

TMR can be seen experimentally with a simple resistance versus applied magnetic field measurement, such as the one shown in Fig. 2.3. Here an applied magnetic field (collinear with the magnetization of the ferromagnetic layers) is swept until the free layer flips into the direction of the applied field (seen where the resistance jumps in magnitude) and then the field is swept back until the free layer returns to the P state. This is a measurement of the so-called minor hysteresis loop, while the major hysteresis loop measures the reversal of both magnetic layers. The minor hysteresis loop is more pertinent to MTJ memory related research where only the reversal of the free layer is desired.

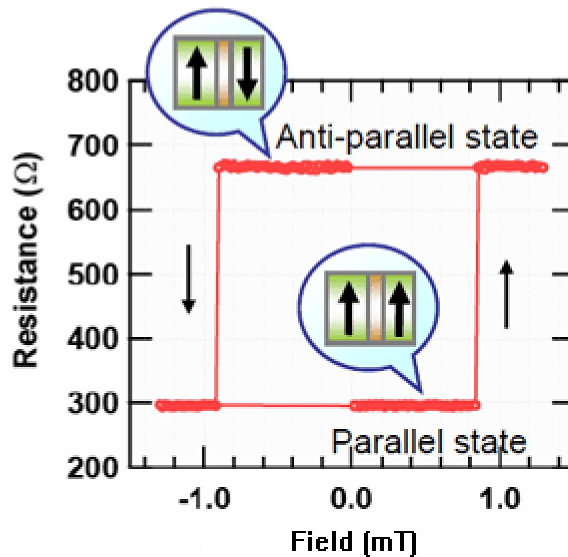

Figure 2.3: Resistance vs. applied field for a MTJ, with each resistance state's magnetic configuration shown in their respective callouts. From wpi-aimr.tohoku.ac.jp.

In the resistance vs. field measurement, the free layer is flipped by the applied magnetic field causing a change in the energy landscape for the magnetization direction, illustrated in Fig. 2.4, so that only one global minima (i.e. stable magnetization configuration) exists. This

is one method of switching the free layer magnetization direction of a MTJ. The following two sections will discuss spin-transfer torque and the faster, more energy efficient method of switching it provides.

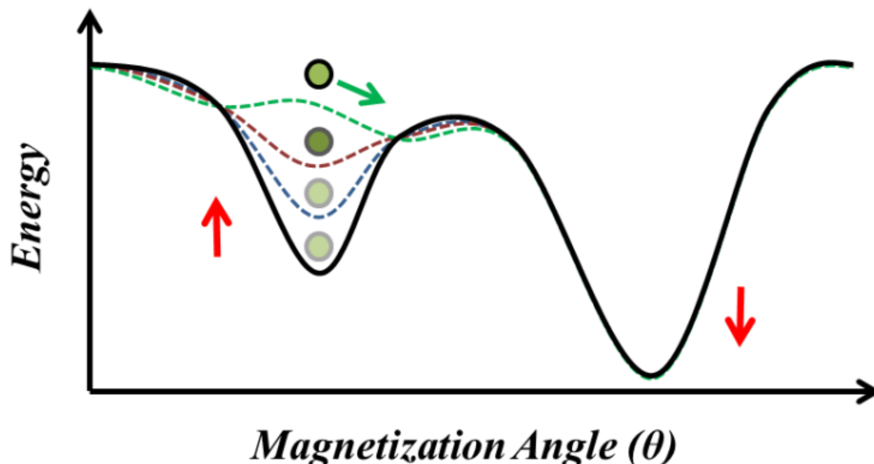

Figure 2.4: Energy of the free layer versus magnetization angle during a reversal. As the magnetic field increases, one magnetization alignment becomes more and more energetically preferred until only one global minima exists. From [6].

2.3 Spin-Transfer Torque

Another quantum effect that arises in a ferromagnet|insulator|ferromagnet system is also based in the electron's spin. First theoretically proposed by Slonczewski [7] and Berger [8], spin dependent scattering in magnetic structures such as MTJs causes angular momentum transfer from the electron current to the magnetization of the ferromagnetic layers. One can take the incoming electrons to be in a superposition of basis states $|\uparrow>$ and $|\downarrow>$, and then assume as Slonczewski that the up and down components are either totally transmitted or reflected at the ferromagnet|insulator interface. In this way, the current becomes polarized both in the forward and reverse directions (with respect to the current polarity) and therefore the ferromagnet must exert a torque on the current. Since angular momentum is conserved in this system, there must also be an equal and opposite torque exerted on the ferromagnet

as denoted by the red arrows in Fig. 2.5a for both transmitted and reflected electrons. This is known as spin-transfer torque (STT), and it has been exploited in the design of magnetic heterostructures such as MTJs so that the torque is capable of inciting major dynamics in one of the ferromagnetic layers (free layer for MTJs). The case of STT acting on a MTJ in Fig. 2.5b shows how the torque acts on the free layer for both polarities of current. Here the electrons polarized by the free layer do not carry enough angular momentum to affect the magnetization dynamics of the fixed layer held in place by an antiferromagnet (AFM in the figure), but often times in practice the fixed layer is anchored by means of a Neél coupling with a nearby ferromagnet in a SAF. In the figure, negative current polarity causes the transmitted spin-polarized electrons to pull the free layer into the direction of the fixed layer while positive polarity causes the reflected spin-polarized electrons to push the free layer away from the fixed layer direction.

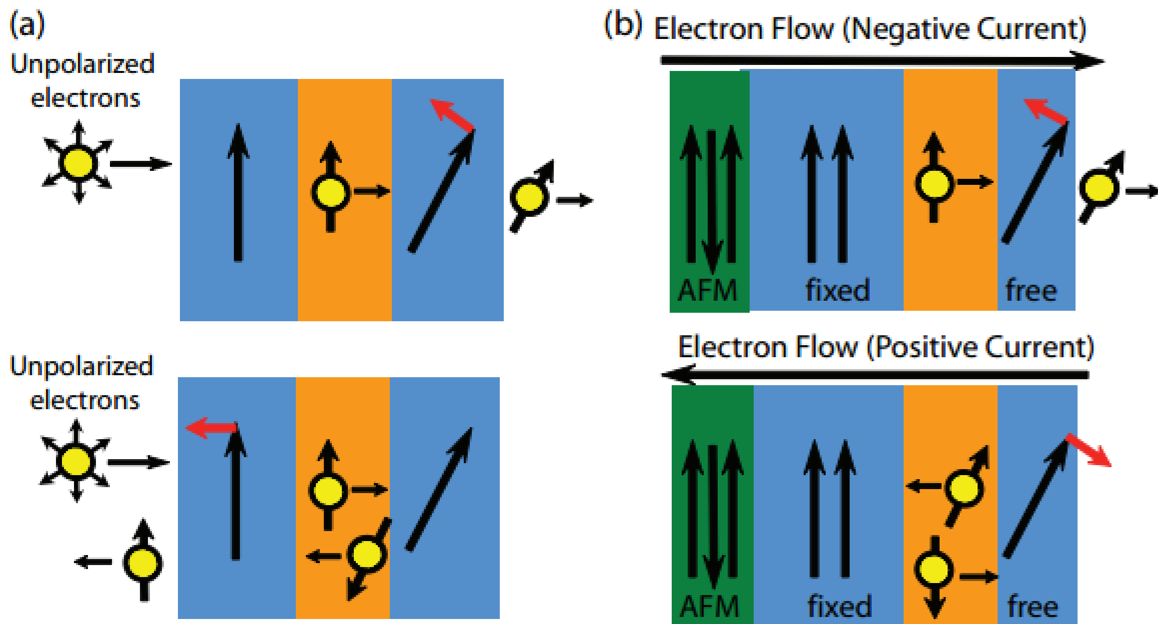

Figure 2.5: A simplified depiction of the spin-transfer torque effect on (a) magnetic layers for electrons both transmitted (top) and reflected (bottom) across the insulator tunnel barrier (yellow) and (b) the free layer of an MTJ for both current polarities (where the red arrows indicate the direction of the spin torque for each polarity). From [9].

STT has experienced a large influx of research in recent years [10, 11] mostly due to the commercial applicability of the dynamics it incites in magnetic multilayers. The two most prominent of these dynamics are stable precession of the magnetization, which has various applications in microwave frequency electronics, and magnetization reversal (switching), which serves as the writing mechanism for the next-generation non-volatile memory STT-MRAM. The following section will cover these magnetization dynamics in more detail, with particular attention paid towards magnetization reversal.

2.4 Spin-Transfer Torque Driven Magnetization Dynamics and Switching

Including the STT effect from the previous section, dynamics of the free layer magnetization of a MTJ $\vec{m}$ in the macrospin approximation (and assuming a fixed magnitude of $\vec{m}$) are governed by the Landau-Lifshitz-Gilbert-Slonczewski (LLGS) equation:

$$\partial_t \vec{m} = -\gamma_0 \vec{m} \times \vec{H}_{eff} + \alpha(\vec{m} \times \partial_t \vec{m}) + \eta \frac{\mu_B I}{e M_s t} \vec{m} \times (\vec{m} \times \vec{p}) \tag{2.6}$$

where γ_0 is the gyromagnetic ratio for an electron, α is the Gilbert damping parameter, η is the spin transfer efficiency, μ_B is the Bohr magneton, e is the electron charge, I is the electrical current, M_s is the saturation magnetization of the free layer, t is the thickness of the free layer, $\vec{p}$ is the directional unit vector of the spin polarization of the current I, and $\vec{H}_{eff}$ is the effective field with the following contributions.

$$\vec{H}_{eff} = \vec{H}_{app} + \vec{H}_{dip} + \vec{H}_{ex} + \vec{H}_{anis} + \vec{H}_{demag} \tag{2.7}$$

where $\vec{H}_{app}$ is the externally applied field, $\vec{H}_{dip}$ is the dipole field from the fixed layer, $\vec{H}_{ex}$ is the exchange field arising from the system trying to minimize its micromagnetic curvature,

$\vec{H}_{anis}$ is the anisotropy field originating from shape, surface, and crystalline effects, and $\vec{H}_{demag}$ is the demagnetization field arising from the system trying to minimize the magnetic surface charges built up on the boundaries of the free layer (giving rise to an effective shape anisotropy). It is this shape anisotropy in the form of the demag field that creates a uniaxial anisotropy along the long axis of an elliptical nanopillar MTJ. This forces the magnetization of ferromagnetic layers to align in either direction of the energetically preferred axis, or easy-axis. As seen from the first term of equation 2.6, the free layer magnetization will align with $\vec{H}_{eff}$ in equilibrium. But given a small perturbation away from equilibrium, the first term causes the magnetization to precess around the effective field. The second term of 2.6 acts as a damping torque that tends to pull the free layer magnetization back toward the effective field, which is broadly due to spin-orbit coupling to the lattice of the free layer [12]. The last term of 2.6 is the contribution to the dynamics from STT, which acts collinear with the damping and its polarity is determined by the direction of current passing through the device I and the spin polarization direction $\vec{p}$. For MTJs, the spin polarization direction is controlled by the fixed layer magnetization, where electron spins are polarized to align with the direction of the fixed magnetization. Therefore, the direction of current determines whether the STT acts parallel or antiparallel to the damping torque. The relative directions of precession and torques are shown in Fig. 2.6 for clarity.

Under the influence of STT, magnetization dynamics proceed in one of three general trajectories determined by the magnitude and polarization of the applied current, seen in Fig. 2.7. Since the magnetization of the free layer is set to be conserved, it's motion can be represented by paths on a unit sphere. When the STT acts against damping but is smaller in magnitude, the magnetization follows a damped motion and returns to equilibrium. When the STT balances out the damping torque by the application of a high current density, the magnetization stably precesses at its natural GHz-level frequency described by the solution to 2.6. When the STT greatly exceeds the damping torque with an even larger current density (the regime of primary interest to this work), the free layer magnetization preces-

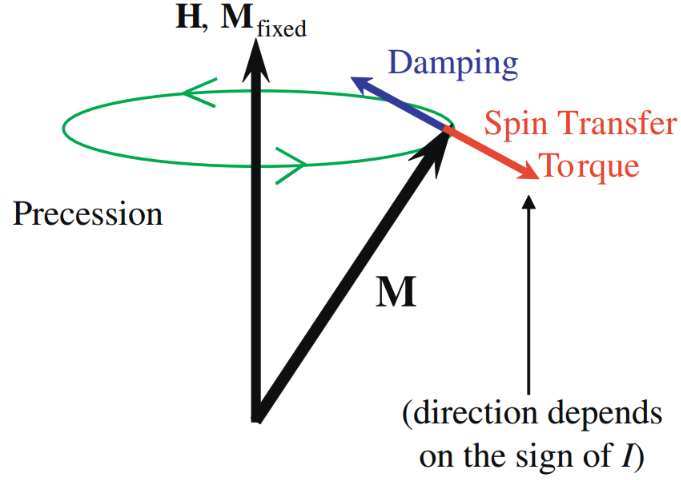

Figure 2.6: Magnetization dynamics of a free layer M, precessing around an effective field H aligned in the direction of the fixed layer M_{fixed}, under the influence of damping that pulls the free layer magnetization in the direction of the effective field and spin-transfer torque that pulls or pushes the magnetization collinear to the damping depending on the polarity of the spin-current. From [11].

sion grows until it rotates into the opposite hemisphere, where the STT then acts to aid damping and stabilize the magnetization towards the new local energy minima. This results in a 180°reversal of the free layer, or "switch" of the magnetization state. In the case of in-plane MTJs, this threshold current density (known as the critical current density J_c) can be derived from a solution to 2.6 and expressed as [13]:

$$J_c = \frac{2e}{\hbar}\frac{\alpha M_s t}{\eta}(H_{app} + H_{anis} + \frac{H_{demag}}{2}) \tag{2.8}$$

where $\hbar$ is the reduced Planck constant and all other variables and constants have been defined previously. This method of using a current to switch the magnetization state of a MTJ has been heavily researched because its optimization is necessary for STT-MRAM to be commercially competitive [10]. Equation 2.8 is calculated at zero temperature and does not take into account thermal effects that might influence switching behavior. The Néel-Brown model of magnetization reversal takes into account thermal fluctuations of the magnetization and the effect they plan in switching a single domain ferromagnetic layer [14, 15]. Such

behavior has been experimentally observed for single domain size ferromagnets [16], where the probability of switching (now that thermal excitations make the behavior much more probabilistic) of a MTJ free layer is proposed to be [17]:

$$P_{switch} = 1 - exp\left[\frac{t_p}{\tau_0} exp\left(-\frac{E_B}{k_B T}\left(1 - \frac{V}{V_c}\right)\right)\right] \tag{2.9}$$

where t_p is the duration of the applied voltage pulse used to switch the device, τ_0 is the attempt period (usually taken to be 1 ns [16]), E_B is the energy barrier between the two stable states, k_B is the Boltzmann constant, T is the temperature, V is the applied voltage, and V_c is the critical voltage corresponding to the critical current in 2.8.

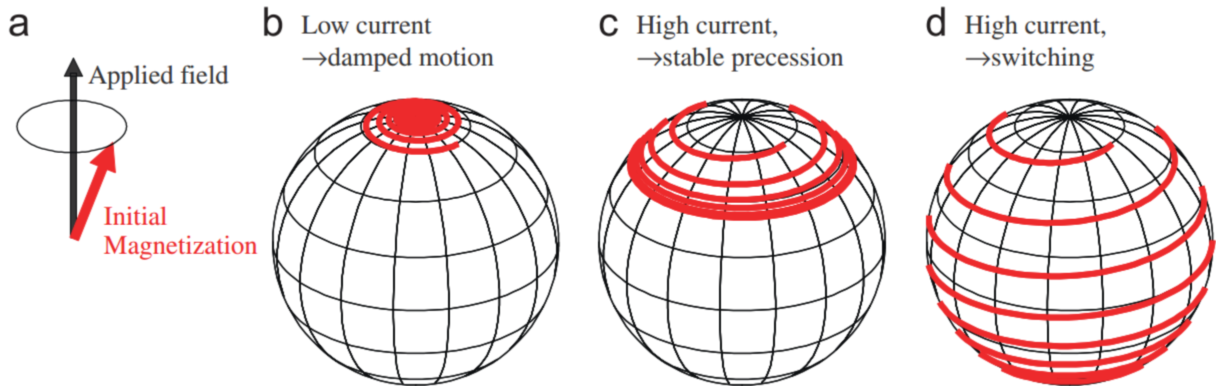

Figure 2.7: Precession of magnetization for different spin-torque regimes produced from increasing the injected current into the MTJ. From [11].

With this chapter's understanding of the physics behind MTJ behavior, the remainder of the thesis will focus on characterization techniques (and a discussion of the results they produce) used to investigate device properties deemed by this chapter as pertinent to MTJs use in STT-MRAM.

Chapter 3

Experimental Procedures

This chapter describes techniques used to investigate MTJ properties for STT-MRAM, the first being more general to the MTJs magnetodynamics while the latter applying more directly to MTJs use as STT-MRAM. Before diving straight into these measurement techniques, a note should be made about the overall approach to conducting experimental research. Before implementing any experimental technique, one should have a clear understanding of the procedure and the equipment/devices used in the experiment. This includes knowing every step of the process (and comprehending the reason for each step) $before$ beginning the experiment, as well as awareness of the necessary safety protocols for the equipment and devices involved. Furthermore, one should be perpetually mindful of every movement and action taken, which includes thinking through the ramifications of each action. This requires a large amount of focus, often needed for hours at a time. In order to achieve this level of concentration, a good experimental researcher must learn discipline in addition to the knowledge of the experiment itself. An example of needed mindfulness that pertains to the research described in this chapter is electrostatic discharge (ESD) safety. ESD occurs when two objects with a potential difference (usually arising from the accumulation of static charges) come in contact, generating a sudden flow of electricity. The human

body can build-up static charges yielding a potential well over a Volt, more than enough to cause dielectric breakdown in MTJs or damage equipment on 50 Ohm lines. To prevent ESD, one must effectively ground oneself to the same ground shared by the ESD-sensitive equipment and devices. This can be achieved by wearing a grounding strap connected to a power outlet (the circular hole in US 3-prong outlets) on the same power line as the equipment and devices whenever contacting these objects. Furthermore, one should also be aware of and minimize all static charge inducing actions such as dragging one's feet while walking or standing up from a cloth seat. This example offers a good indication of the constant alertness and attention to detail necessary for conducting proper experimental research.

3.1 Field Modulated Spin-Torque-Driven Ferromagnetic Resonance

As described in Chapter 2, a magnetic moment will stably precess at an intrinsic frequency around an effective applied field in the absence of damping. Section 2.4 further states that application of spin-torque from a spin polarized current to a magnetic moment acts as damping or anti-damping depending on the polarity of the current. Combining these two effects with a MTJ's resistance depending upon the relative orientation of the magnetization directions of the fixed and free layer (section 2.2), one can create a method to extract meaningful information about MTJ characteristics.

First reported by Tulapurkar et al. [18], applying an AC microwave current near the resonance frequency of either magnetic layer incites precession of the magnetization, and therefore oscillation of device resistance, whose mixing AC current and voltage produce a measurable rectified DC signal. This technique, appropriately named spin-torque-driven ferromagnetic resonance (ST-FMR), allows for electrical measurement of magnetic dynamics at the level

of individual nanometer-scale MTJs [19–24] . This section will introduce an improvement to this technique, known as field modulated spin-torque-driven ferromagnetic resonance (FM ST-FMR) [25], whose origins will now be described in detail.

An alternating radio frequency (RF) spin polarized current applied near the resonance frequency can drive the precession of magnetization by effectively pushing and pulling the magnetization (depending on the instantaneous polarity of the RF current) in phase with its natural precession. In the case of MTJs, the fixed layer acts as a spin filter which polarizes the current passing through the free layer in the direction of the fixed layer's magnetization. In this discussion, it is assumed that the fixed layer magnetization is ideal and completely locked in place. This oscillation of the free layer magnetization will also produce an oscillation of the device resistance due to the varying relative angle between fixed and free layer magnetizations (and TMR's dependence on said angle; see section 2.2). The time-dependent resistance can be expressed as the expansion [19]:

$$R(t) = R_0 + \Delta R(t) = R_0 + Re(\sum_n \Delta R_{nf} e^{in2\pi ft}) \tag{3.1}$$

where ΔR_{nf} can be complex. Since the fixed layer is supposed to be stationary, the resistance thus oscillates as the magnetization of the free layer m, which is the solution of the LLGS equation 2.6. The product of this AC resistance and the applied AC current that creates it yields a rather complicated rectified voltage, which was calculated by Wang et al. for

in-plane magnetized MTJs in the macrospin approximation as [20]:

$$
\begin{aligned}
V_{mix} = & \\
& \frac{1}{4}\frac{\partial^2 V}{\partial I^2} I_{rf}^2 \\
& + \frac{1}{2}\frac{\partial^2 V}{\partial\theta\partial I}\frac{\hbar\gamma_0 \sin\theta}{4eM_s\mathcal{V}\sigma} I_{rf}^2(\varepsilon_\parallel S(\omega) - \varepsilon_\perp \Omega_\perp A(\omega)) \\
& + \frac{1}{4}\frac{\partial^2 V}{\partial\theta^2}(\frac{\hbar\gamma_0 \sin\theta}{4eM_s\mathcal{V}\sigma})^2 I_{rf}^2(\varepsilon_\parallel^2 + \varepsilon_\perp^2\Omega_\perp^2)S(\omega) \\
& + \frac{3}{8}\frac{\partial V}{\partial\theta}\frac{H_{anis}\sin 2\beta}{H_z + H_{anis}\cos 2\beta}(\frac{\hbar\gamma_0 \sin\theta}{4eM_s\mathcal{V}\sigma})^2 I_{rf}^2(\varepsilon_\parallel^2 + \varepsilon_\perp^2\Omega_\perp^2)S(\omega) \\
& + \frac{\partial V}{\partial\theta}\frac{1}{M_s\mathcal{V}(H_z + H_{anis}\cos 2\beta)}[\frac{1}{4}\frac{\partial^2\tau_\perp}{\partial^2\theta} I_{rf}^2 \\
& + \frac{1}{2}\frac{\partial^2\tau_\perp}{\partial\theta\partial I}\frac{\hbar\gamma_0 \sin\theta}{4eM_s\mathcal{V}\sigma} I_{rf}^2(\varepsilon_\parallel S(\omega) - \varepsilon_\perp \Omega_\perp A(\omega)) \\
& + \frac{1}{4}\frac{\partial^2\tau_\perp}{\partial^2\theta}(\frac{\hbar\gamma_0 \sin\theta}{4eM_s\mathcal{V}\sigma})^2 I_{rf}^2(\varepsilon_\parallel^2 + \varepsilon_\perp^2\Omega_\perp^2)S(\omega)]
\end{aligned}
\tag{3.2}
$$

Here γ_0 is the gyromagnetic ratio, $M_s\mathcal{V}$ is the total magnetic moment of the free layer, H_{anis} is the in-plane anisotropy value for the free layer, H_z is the component of magnetic field acting on the free layer along the equilibrium direction of the layer (this includes the applied field as well as the dipole field but not the demagnetization field), β is the in-plane angle between the equilibrium direction of the precessing layer and the magnetic easy axis, θ is the in-plane angle between fixed and free layer magnetizations, $\tau_\perp$ is the perpendicular component of the spin-torque vector, I_{rf} is the applied microwave frequency current,

$$
\Omega_\perp = \gamma_0 \frac{4\pi M_{eff} + M_{eff}(H_z - H_{anis}\sin^2\beta)}{\omega_m} \tag{3.3}
$$

where ω_m is the resonance frequency of the precessing layer and $4\pi M_{eff}$ is its effective out-of-plane anisotropy,

$$
\varepsilon_{\parallel,\perp} = \left[\frac{2e/\hbar}{\sin(\theta)}\right]\frac{d\tau_{\parallel,\perp}}{dI} \tag{3.4}
$$

are the dimensionless in-plane (∥) and out-of-plane (⊥) differential torques, and $S(\omega)$ and $A(\omega)$ are symmetric and anti-symmetric lorentzians of the form:

$$S(\omega) = \frac{1}{1 + \frac{(\omega-\omega_m)^2}{\sigma^2}} \tag{3.5}$$

$$A(\omega) = \frac{\frac{\omega-\omega_m}{\sigma}}{1 + (\frac{\omega-\omega_m}{\sigma})^2} = \frac{(\omega - \omega_m)}{\sigma} S(\omega) \tag{3.6}$$

where ω_m is the previously mentioned resonance frequency and σ is the linewidth of the resonance peak given by:

$$\sigma = \frac{\alpha\gamma_0 M_{eff}}{2}(4\pi + \frac{2H_z + H_{anis}(\cos^2\beta - 2\sin^2\beta)}{M_{eff}}) - \frac{\gamma_0}{2M_s\mathcal{V}}\frac{\partial\tau_{\parallel}}{\partial\theta} \tag{3.7}$$

Given the complexity of 3.2, fitting that behemoth of an equation (and all its necessary parameters) to experimental data can be quite the herculean task and even then there is a lack of agreement in the field about its results [22,26]. However, one can greatly simplify V_{mix} and still extract two very important parameters (ω_m and σ) for characterizing MTJs. To do this, one can fit V_{mix} to a linear combination of symmetric and anti-symmetric lorentzians:

$$V_{mix} = V_s S(\omega) + V_a A(\omega) \tag{3.8}$$

where V_s and V_a are functions of the spin-torque vector and other magnetic parameters. In this case, fitting is much more straightforward as only four parameters need to be fit per resonance curve. One can then study the resonance frequency and linewidth as function of another controllable parameter (such as applied field) and compare with theoretical models to extract useful magnetic information like anisotropy field or Gilbert damping parameter. To this end, one can measure the resonance frequency of an in-plane elliptical MTJ as a function of easy-axis applied field (other measurement geometries would also be acceptable,

but this particular set-up will be the focus of this work) and fit to the Kittel equation [27]:

$$\omega_m = \gamma_0 \sqrt{H_{app}(H_{app} + H_k + 4\pi M_s)} \tag{3.9}$$

where H_{app} is the total easy-axis applied field (including in-plane anisotropy field and dipole field) and H_k is the uniaxial out-of-plane anisotropy field. Since saturation magnetization M_s is well known for different materials, only a single parameter fitting is needed to extract H_k, which plays a critical role in an MTJ's energy barrier (and therefore stability). Using the same measurement configuration as above, one can take the extracted linewidth (defined in this case as half-width at half-maximum, HWHM) as a function of easy-axis applied field, linearly extrapolate to find the zero-field linewidth, and use the following approximation from Sankey et al. [19] to find the zero-field Gilbert damping parameter:

$$\alpha = \frac{\sigma_0}{f_0} \tag{3.10}$$

where ω_0 is the zero-field linewidth and f_0 is the zero-field resonance frequency (notice not angular frequency). Damping is one of the most important parameters used in MTJ characterization because the critical current scales linearly with damping and minimization of the critical current (and therefore switching current) is essential for STT-MRAM commercialization. Although these two fitting techniques are simple in principle, measuring ST-FMR in the easy-axis geometry is rarely performed. This is because the collinear magnetizations of the free and fixed layers in the easy-axis geometry produce minimal spin-torque and, in turn, minimal signal. In conventional ST-FMR measurements, the RF current is pulsed on and off at some low kHz frequency and then voltage is measured with a lock-in amplifier in order to hone in on the signal, known as amplitude modulation. This technique also suffers from a frequency-dependent non-magnetic background as well as standing waves, both inherent to the electrical measurement that dominates the signal and usually has to be removed during data analysis. It would seem that the problem with amplitude modulation is that it

is unable to remove the large electrical background that hides the easy-axis signal. Enter FM ST-FMR. As denoted in its name, FM ST-FMR modulates the applied magnetic field (also at low kHz frequency) instead of the AC current, as done in conventional ST-FMR, and still measures the rectified voltage. The modulation field of a few Oersteds is provided by a copper wire passing a kHz-level sinusoidal current of a few Amperes placed directly above the MTJ, along the hard-axis direction [25]. The Oersted field produced by the current is collinear with the DC applied field. By modulating the field, only signals that are dependent on magnetic field are measured, effectively removing the parasitic non-magnetic background. The measured signal $\widetilde{V}_{mix}$ is actually the change in the rectified voltage V_{mix} with respect to the modulated quantity, the applied field H

$$\begin{aligned}\widetilde{V}_{mix} = H_{rms}\frac{\partial V_{mix}}{\partial H} = H_{rms}\Bigg[\frac{\partial V_s}{\partial H}S(\omega) + \frac{\partial V_a}{\partial H}A(\omega) \\ + \frac{1}{\sigma}\frac{\partial \sigma}{\partial H} \times \left(2V_s A^2(\omega) + V_a\big[2\frac{A^3(\omega)}{S(\omega)} - A(\omega)\big]\right) \\ + \frac{1}{\sigma}\frac{\partial \omega_m}{\partial H}\left(2V_s S(\omega)A(\omega) + V_a\big[A^2(\omega) - S^2(\omega)\big]\right)\Bigg]\end{aligned} \tag{3.11}$$

where H_{rms} is the RMS amplitude of the modulation field at the sample. This is the equation to be fitted for FM ST-FMR, which consists of 8 parameters (6 prefactors, ω_m, and σ) from a linear combination of 6 lorentztian-like terms. Example spectra and direct comparison between the two techniques is shown in Fig. 3.1, where the same measurement is taken with both techniques in the easy-axis configuration. It is clear from this juxtaposition that field modulation allows for the observation of a much richer spectrum of magnetic dynamics. With this new technique, the non-magnetic background and standing waves are greatly diminished and there is an order of magnitude improvement in the signal-to-noise ratio (SNR). Now with the above understanding of the signal, the remainder of this section will describe the

measurement procedure to attain this rectified signal.

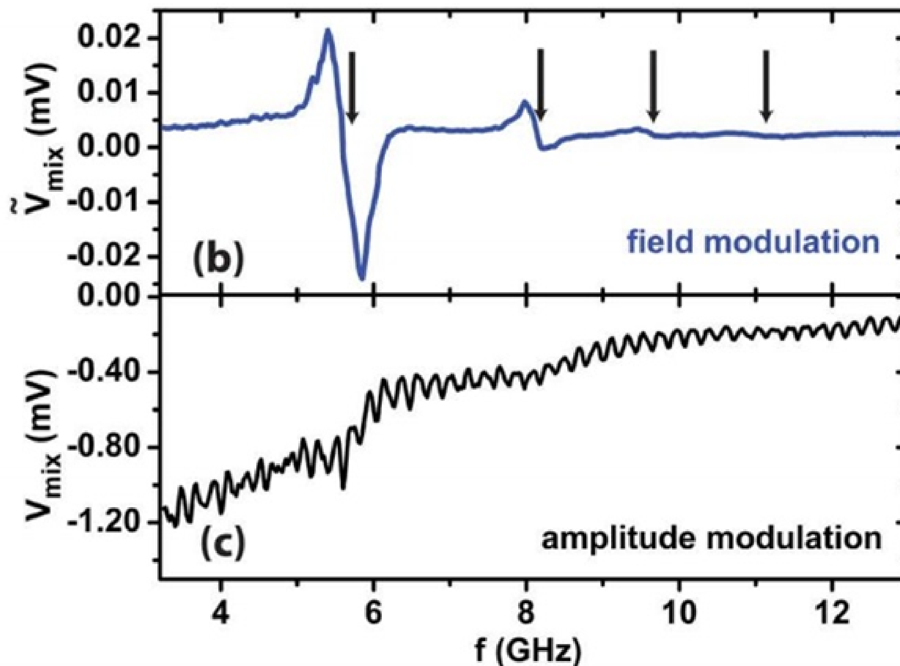

Figure 3.1: Comparison of typical ST-FMR spectra taken with field modulation (top) and amplitude modulation (bottom) in the easy-axis configuration. The black arrows in the top spectra identify four different resonance peaks, while barely one is visible with amplitude modulation. From [25].

The relatively simple circuit employed for FM ST-FMR is shown in Fig. 3.2. It involves a microwave generator supplying an RF current through the AC port of a bias tee and a lock-in amplifier measuring the voltage through the DC port of the bias tee. A copper modulation wire is placed directly over the device under test and a sound amplifier drives Ampere-range current at a few kHz frequency through the wire. For example, this work employed a Agilent E8257D microwave signal generator, Signal Recovery 7225 DSP lock-in amplifier, and Behringer Europower EP4000 Stereo Power Amplifier. Since the resistance of the wire is minimal, a high-Watt resistor (not shown) needs to be placed in series with the modulation wire to dissipate heat and provide enough resistance for impedance matching the line (only a few Ohms are necessary). The lock-in provides the reference signal for the

modulation field. A microwave probe is used to make electrical contact with the device; hence a microwave probe station is needed. The following procedure is employed to implement the measurement:

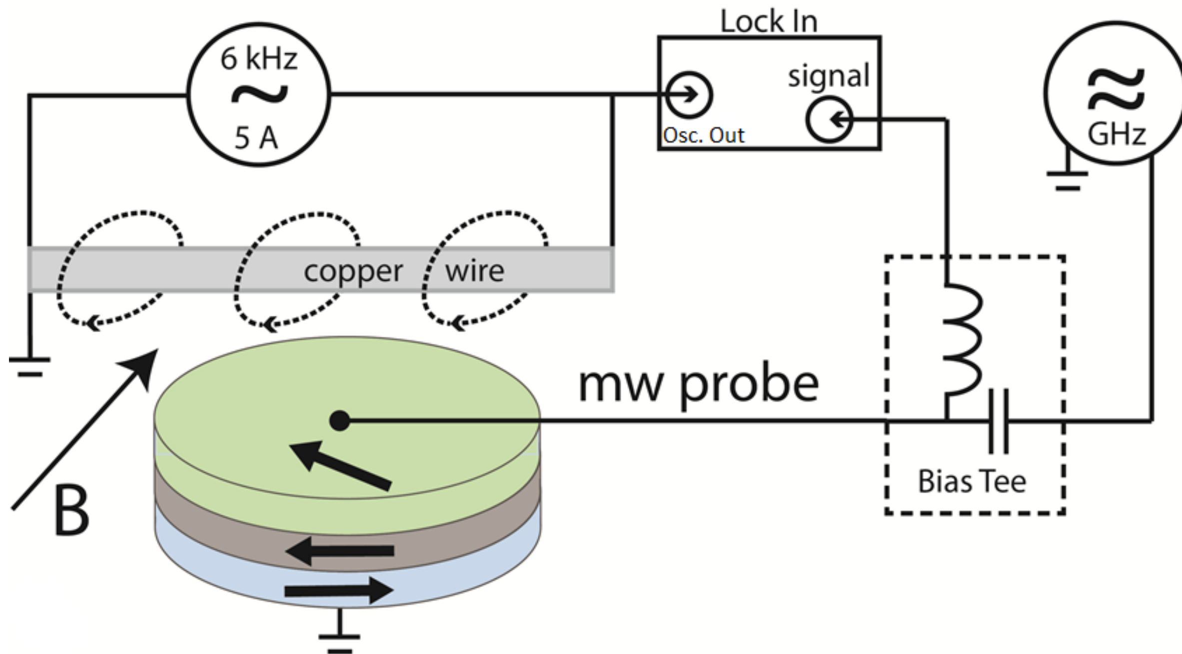

Figure 3.2: Depiction of the FM ST-FMR circuit with enlarged illustration of the field modulation wire placed over the device under test. From [25].

1. Connect the RF output of the microwave generator to the AC port of the bias tee.

2. Connect the input of the lock-in amplifier to the DC port of the bias tee and then connect the microwave probe (and sample) to the AC/DC end of the bias tee. If a DC bias is desired, also connect it to the DC port of the bias tee via a BNC tee.

3. Set the lock-in input to the appropriate channel, set the sensitivity to roughly the same amount as the peak-to-peak signal intended to be measured (usually between 10 and 100 μV), adjust the AC gain accordingly, set the reference source to internal and at 5003 Hz (or another low-kHz prime number frequency). Do not set the phase as it will be handled in post-processing.

4. Connect the reference output (Osc. Out in the diagram) to the input of the sound amplifier.

5. Connect the sound amplifier output to the high-Watt resistor in series with the modulation wire. A multimeter can be connected in series to monitor the current and frequency.

6. Place the modulation wire directly above ($< 1cm$) the device under test so that the wire's length runs along the in-plane hard-axis of the device. This way the modulation field generated will be collinear with the easy-axis and applied static field.

7. Turn on the sound amplifier and let it warm up for a minute or two. Then, slowly ramp up the current ($< 0.5Amps/sec$) to the desired level. For reference, this work employed a 4.7 Ohms 1 kW resistor with an RMS current of roughly 5 Amperes. With this configuration, the resistor becomes hot enough to burn skin and should be placed safely away from heat sensitive equipment. Also given the high current, an individual must always be present when the modulation circuit is in use.

8. Now measurement can begin. Set the applied static field to the desired value and sweep the applied RF current in frequency through the resonance condition (this is known as the frequency domain) while measuring the voltage with the lock-in. One can also set the RF current and sweep the field (known as the field domain), but interpretation of the data in this configuration can be difficult due to complications such as dragging effects [28] and therefore this work focuses on the frequency domain.

9. When sweeping the frequency, a step size should be used to allow for proper fitting of the FMR peaks with 3.11. A good rule of thumb is to collect at least 10 data points per resonance peak, or in other words the step size should be at least an order of magnitude smaller than the total width of the peak measured (usually a 20 MHz step size will suffice).

An automation software such as LabVIEW can be used to coordinate the equipment, sweep across the necessary parameters, and record the data from the lock-in. The lock-in should output the data in three parts: X component, Y component, and magnitude. X and Y are the cosine and sine component of the magnitude, where the phase of the lock-in measurement is the angle. For proper data fitting, one wants the signal to be maximized in one component and necessarily minimized in the other. Therefore, the phase needs to be adjusted until the previously stated condition is met. This can be done with a fairly simple script that reads the three columns of X, Y, and Mag data, numerically minimize one channel such that the other is maximized as a function of the phase angle, and perhaps have a basic GUI to allow for manual adjustment of the phase for situations where minimization fails or controllable adjustment is desired. An example python script that performs these operations is provided in the Appendix B.

Lastly, a note about the RF power should be made. Since no amplitude information is involved in the fitting procedure described in this section, proper applied power calibration is not necessary and the actual microwave power delivered to the device does not have to be known exactly. Therefore, the only factors that go into the determination of the applied RF power are the following: it isn't enough to switch the magnetization state or cause dielectric breakdown (seen as a discontinuous jump in the measured voltage signal), it creates a signal large enough to be fitted (lineshape is clearly defined and ten points per peak guideline stated previously is met), and it is small enough that it resides in the linear regime where the fitting equations still apply (the regime where peak amplitude over I_{rf}^2 is constant as a function of applied RF power). As a point of reference, this work mainly used an applied power (coming out of the microwave generator) of -2 to -10 dBm for devices with resistances in the low-kΩ regime.

3.2 Write Error Rates

When characterizing MTJs for use as computer memory elements (i.e. individual bits), certain metrics need to be established to quantify their performance as such. The two most basic operations necessary for binary computer memory are measuring the current state of the bit (read) and setting the bit to a desired state (write). For STT-MRAM, the read operation can be carried out by a simple resistance measurement. A significant complication inherent to the read operation is that the voltage applied to measure the resistance, although small, might be enough to switch the current state of the device. The probability of the device switching states for a given applied read voltage is known as the read disturb rate (RDR). Since the RDR is, to first order, exponentially dependent on applied voltage [29], minimizing the read voltage (i.e. $V_{read} \ll V_{c0}$) is an effective method to eliminate RDR. However, the write operation is much more crucial to memory performance metrics as it tends to be the bottleneck for speed and energy consumption and therefore its adoption in industry [10]. In the case of STT-MRAM, ”writing” a bit is performed by reversal of the free layer via a large spin polarized current. In functional terms, this means applying a ”write pulse” that in current research is a nanosecond scale voltage applied across the MTJ. A vital factor for memory operation is the reliability of each write attempt. The associated metric of this reliability is known as the write error rate (WER), which is defined as:

$$WER = \frac{N_{NoSwitch}}{N_{SwitchAttempts}} \tag{3.12}$$

or in other words, the probability of a given write attempt being unsuccessful. In order to be managed by typical error correcting techniques used throughout computer memory, a WER of the order of 10^{-9} is necessary for useful memory application. Therefore, characterizing a device's WER requires very large statistics, which is only increased by taking into account the approximately $\sqrt{N}$ counting error associated with the binary results of switching at-

tempts. Measurement of WER to this degree would take years with university-level research equipment. To overcome this issue, WER can be measured up to the 10^{-6} (or some other intermediate value) and extrapolated. The remainder of this section describes a procedure developed to quickly and accurately measure WER with large statistics as a function of a particular parameter.

To determine the success of a switching attempt, one must know the state of the device before and after the write pulse. After the switching attempt, the device must be reset to its original state before the next attempt, usually implemented by a pulse of opposite polarity to the write pulse. Following this logic, a single pulse train (see Fig. 3.3) could perform all of the necessary actions for each switching attempt.

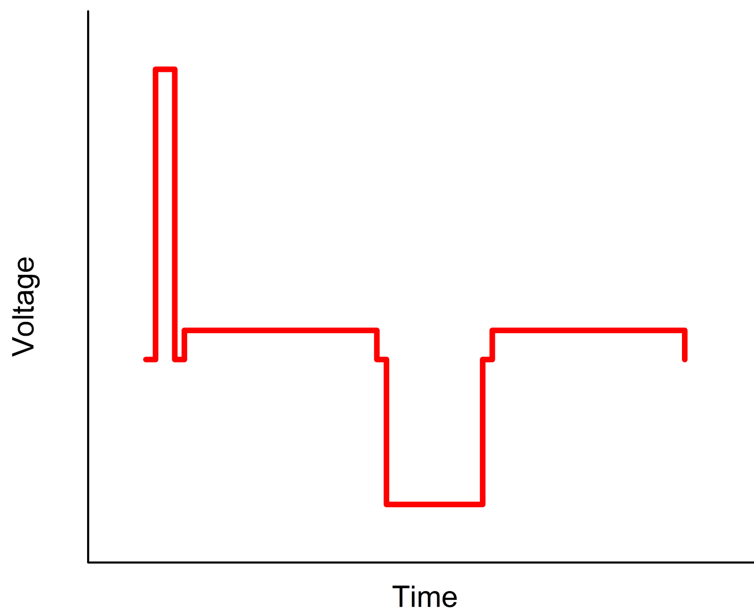

Figure 3.3: Pulse train used for each switching attempt. The order of the pulses is write, read, reset, read. Voltage and time not to scale.

In this particular set up, a Picosecond Pulse Labs 10,0070A pulse generator (PSPL) supplies the write pulse and an Agilent 33220A Arbitrary Waveform Generator (ARB) supplies the

reset pulse. An effective read pulse is implemented by a constant (but small) DC bias voltage supplied by a Keithley 2400 Source Meter (Keithley) and then measured by National Instruments USB-6251 BNC Digital Acquisition Board (DAQ) in between each write and reset pulse. This implementation is necessary due to the measurement circuit, which will be introduced later in this section. The PSPL can supply pulses ranging from 100 picoseconds to 10 nanoseconds, while the ARB has a pulse range from 50 nanoseconds to DC (although most reset pulses used are in the range of hundreds of nanoseconds). The length of the read pulse is limited by measurement speed and accuracy of the DAQ, setting a lower limit of roughly 100 microseconds. This limitation is set at the hardware level and therefore unavoidable with the given resources, but could be improved in future work with the use of better equipment. An appropriate microwave probe station is also used to physically secure and make electrical contact with the device under test, as well as apply a tunable magnetic field (usually via an electromagnet).

Any cyclic permutation of the pulse order in Fig. 3.3 would also work, but this particular ordering is determined by the necessary synchronization (and therefore triggering) of the equipment controlling said pulses as well as the measurement circuit whose block diagram is shown in Fig. 3.4. To ensure proper synchronization, the following procedure is carried out:

1. Connect the trigger output of the PSPL to the trigger input of the ARB. For the particular model of ARB stated earlier, this port is labeled Ext. Trig., which is located on the rear panel.

2. Set the PSPL trigger method to Internal with a repetition rate appropriate for the length of pulse train used (for the work presented in this thesis, 2.5 kHz was used). This method allows the PSPL to control the remaining instruments.

3. Set the ARB trigger to Ext. Trig. (rising edge) and the output mode to Burst.

4. Connect the trigger output of the ARB (labeled "Sync") to the trigger input of the

DAQ, labeled APFI0 (analog programmable function interface) for the model mentioned above.

5. Set the DAQ trigger to APFI0 and the sampling rate to maximum (1.25 MSamples/s in the case of this DAQ)

6. Connect the DC Bias to a reference resistor (approximately equal to the average device resistance) and then connect the reference resistor to the DC port of the bias tee. The DC bias should output constantly for the entirety of the measurement and have a polarity such that it favors the successfully switched state.

7. Connect an analog input of the DAQ (any will do) between the reference resistor and the bias tee.

8. Connect the outputs of the PSPL and ARB, with appropriate attenuators to protect the equipment at the hardware level (for the equipment and circuit used here, -6 dB and -3 dB respectively), to the power divider. Then connect the remaining port of the power divider to the AC port of the bias tee. All connection cables used should be rated for the appropriate frequency of the pulses.

Using the above protocol, enabling the PSPL initiates the entire switching attempt process, repeated at the chosen frequency of the PSPL's internal trigger and recorded by the DAQ. One can implement this entire procedure (with the exception of creating the physical circuit) using an automation software such as LabVIEW. With this approach, LabVIEW will end up with a voltage trace of many switch attempts. In the scope of the large amount of statistics necessary for this measurement, LabVIEW is unequipped to handle the high speed data analysis necessary to measure and process in a reasonable timescale. Therefore, it is much more time efficient to have LabVIEW extract the two sections of each switch attempt corresponding to the read pulses, average over the length of the each pulse, and write these before and after voltages to a file that can be post-processed later by faster data analysis

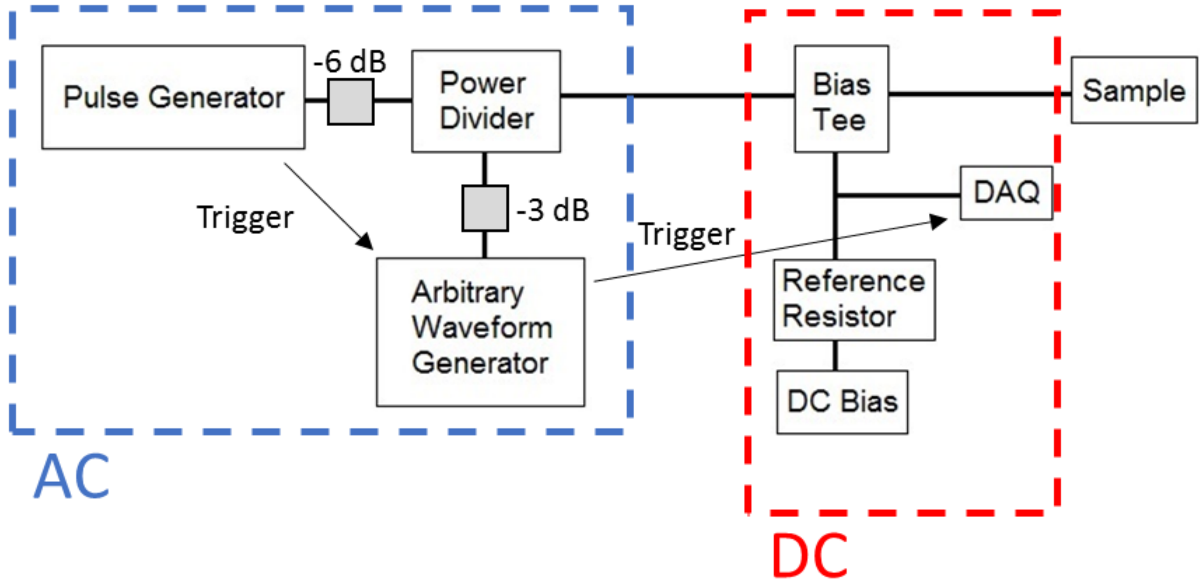

Figure 3.4: WER Circuit. By combining ARB and PSPL outputs (via a power divider/combiner) into the AC port of the bias tee and the voltage measurement component (realized as a voltage divider) into the DC port, the AC and DC components are effectively isolated. This allows for minimally distorted write and reset pulses applied to the device as well as a simple DC circuit to evaluate resistance.

software. This method yields a long list of initial and final voltages from each switch attempt that can be translated into resistances and compared to evaluate the success of each attempt. Keep in mind that there will be an offset due to the ordering of the pulse train (i.e. one needs to compare the second read pulse of a given pulse train to the first read pulse of the following pulse train in order to compare the state of the device before and after each write pulse).

From the voltage recorded by the DAQ, it is a simple calculation to recover the resistance of the sample. Since the DC part of the circuit is a straightforward voltage divider, the resistance of the MTJ as a function of the measured DAQ voltage V_{DAQ} is given by:

$$R_{MTJ} = \frac{R_{Ref}|V_{DAQ}|}{|V_{read} - V_{DAQ}|} \tag{3.13}$$

where R_{Ref} is the value of the reference resistor in Ohms and V_{read} is the applied DC bias used as the read voltage. Here the importance of V_{read} becomes more apparent. As stated earlier in this section, V_{read} needs to be small enough so that it doesn't read disturb the MTJ and cause an unwanted switch. However, using 3.13 to calculate the measurable voltage difference between resistance states gives:

$$\Delta V_{DAQ} = V_{read} \frac{(R_{AP}R_{Ref} - R_P R_{Ref})}{(R_{AP} + R_{Ref})(R_P - R_{Ref})} \tag{3.14}$$

where R_P and R_{AP} are parallel and antiparallel state resistances of the device, respectively. Here one can see that the measurable difference between states (and therefore the accuracy of differentiating between them) is linearly dependent on the read voltage. One must take into account both of these factors to determine the appropriate V_{read}. As a point of reference, the read voltage used in this work was usually set at 30 mV for devices with average resistances of about 1 to 2 kΩ.

At this point in the procedure, all that remains to be done is determining an adequate reset voltage and processing the raw data output by LabVIEW. To assess the efficacy of the reset pulse, it turns out that one first needs to process some initial data and then optimize based upon the results in an iterative fashion. To this end, the processing will be discussed first. To analyze the raw data file, this work uses a python script that effectively carries out the following routine:

1. Read a given raw data file and extract all initial and final measured voltages (keeping in mind the offset discussed previously).

2. Convert said voltages into resistances using 3.13.

3. Determine the device state for each resistance value. This can be achieved by taking the known parallel and antiparallel state resistances and finding the average R_{avg}. If

$R > R_{avg}$ then the device is in the antiparallel state and if $R < R_{avg}$ then the device is in the parallel state.

4. Compare initial and final resistances for each switching attempt and categorize into three possible scenarios: switched (the device started in the correct state and ended in the opposite state), not switched (the device started in the correct state and ended in the same state), and missed (the device started in the incorrect state).

5. Sum over all switching attempts and output total number of attempts, number in each category, and calculate WER as $\frac{N_{NotSwitched}}{N_{attempts}-N_{missed}}$

The full python script is located in Appendix A. Using this analysis technique along with some preliminary data, one can also determine the necessary reset voltage. The following iterative process can be done to find an effective (and safe from dielectric breakdown) reset voltage:

1. Set the write voltage so that most of the switching attempts are successful (to ensure that the reset pulse is necessary).

2. Set the reset voltage to a safe and small amount. A good rule of thumb is half of the write voltage

3. Run the measurement and process the data. Observe the number of missed events. This is the number of attempts where the device did not reset properly and therefore cannot be counted towards the switching probability.

4. Slowly increase the reset voltage until the number of missed events is less than 1% of total switching attempts.

Since reset pulses are much longer than writes (typical resets are 100-500 ns while writes useful for computer memory application are usually less than 10 ns nowadays) in order to

ensure proper switch back, dielectric breakdown can occur at lower voltages. This is why it is important to use the lowest possible reset voltage while still maintaining effectiveness by means of this ramping up technique. It is necessary to minimize reset errors to a low level ($\sim 1\%$ as noted above) because they cannot be included into the switching statistics and are effectively wasted events.

With the measurement techniques detailed in this section, one can reliably and efficiently study WER as a function of write pulse length & voltage, applied field, or any other interesting parameter. With the procedure and example equipment described in this section, 10^6 switching attempts can be measured in about 8.5 minutes. In order to maintain statistical significance while measuring the low probability tail of WER, a requirement of 100 no switch events per data point was established. The results acquired from these measurement techniques are discussed in Chapter 4.

Chapter 4

Results

Findings from the measurement techniques described previously and their analysis are presented in this chapter. The results reported here are on two representative devices of different types of MTJs (one of each) whose only major difference is the composition of the free layer. One type has $Co_{20}Fe_{60}B_{20}$, referred to as Fe-rich, for the free layer while the other has $Co_{60}Fe_{20}B_{20}$, referred to as Co-rich. More specifically, the Fe-rich device has the layer structure Substrate/3 Ta/40 CuN/3 Ta/40 CuN/3 Ta/10 Ru/5 Ta/15 PtMn/2.3 $Co_{70}Fe_{30}$/0.85 Ru/2.4 $Co_{40}Fe_{40}B_{20}$/MgO (RA 12.4 $\Omega \times \mu m^2$)/1.8 $Co_{20}Fe_{60}B_{20}$/5 Ta/10 Cu/5 Ru/3 Ta/ (numbers in nm) patterned into a 130 x 50 nm^2 elliptical nanopillar with in-plane fixed and free layer magnetizations along the long axis of the ellipse, or easy-axis. The layer structure is illustrated in Fig 4.1. The Co-rich device has a nearly identical layer structure Substrate/3 Ta/40 CuN/3 Ta/40 CuN/3 Ta/10 Ru/5 Ta/15 PtMn/2.5 $Co_{70}Fe_{30}$/0.85 Ru/2.4 $Co_{40}Fe_{40}B_{20}$/MgO (RA 11.9 $\Omega \times \mu m^2$)/1.8 $Co_{20}Fe_{60}B_{20}$/5 Ta/10 Cu/5 Ru/3 Ta/ with the same elliptical pillar size and magnetization configuration as the Fe-rich device.

The minor hysteresis loops for both devices are given in Figs. 4.2 & 4.3. The Fe-rich (Co-rich) device shows an AP state resistance of 1700 Ω (3700 Ω) and a P state resistance of 800

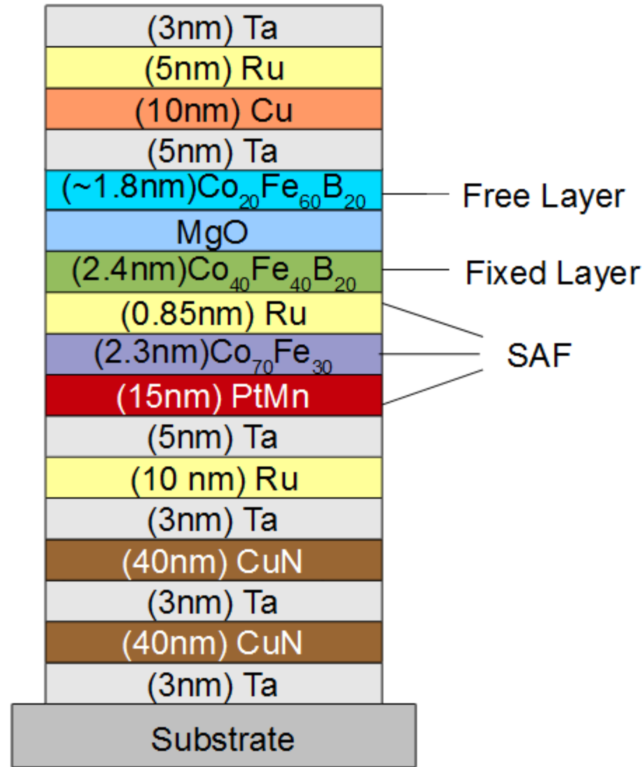

Figure 4.1: Fe-rich MTJ layer structure with the major components labeled.

Ω (2400 Ω) for a TMR ratio of 111% (54%). Both devices have hysteresis widths of about 175 Oe, although with different coercive field offsets due to different SAF influences. To account for this offset, switching measurements were made with an applied field at the middle of each device's hysteresis loop, also known as the switching field. This effectively creates an equivalent energy barrier for the two switching polarities and mimics a calibrated SAF such that the center of the device's hysteresis loop is at zero applied field. This type of calibration would be included in the final version of the MTJs functioning as commercial memory and therefore should be artificially implemented in the characterization process. Both WER and FM ST-FMR measurements were taken for each device. While the Co-rich device behaves in agreement with theoretical predictions, the Fe-rich device displays qualitatively different, anomalous behavior.

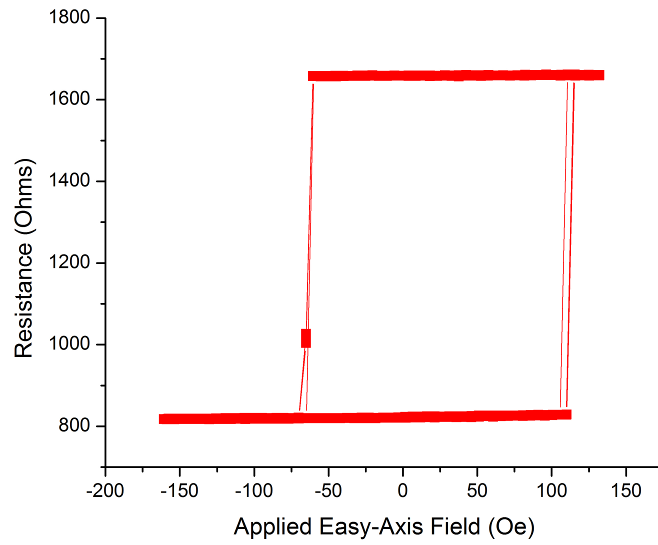

Figure 4.2: Resistance versus field for Fe-rich device

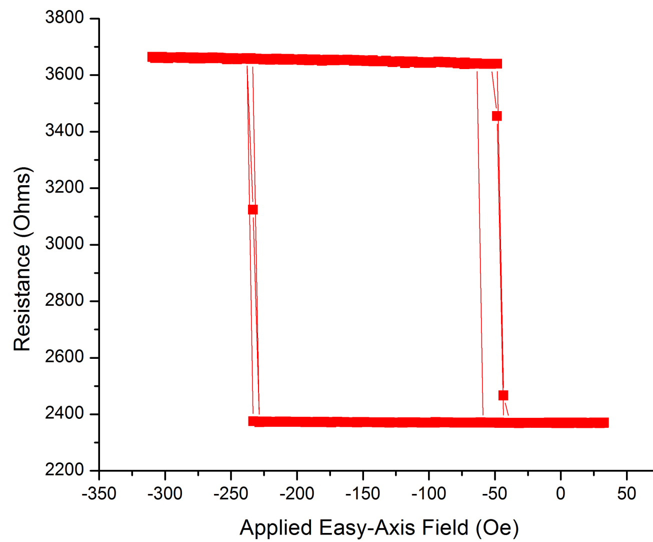

Figure 4.3: Resistance versus field for Co-rich device

WER measurements were made as a function of applied write voltage pulse with a fixed pulse length of 10 ns. For the configuration used in this measurement, positive voltage switches the devices from AP to P state and visa versa for negative polarity. Unless otherwise noted, WER measurements are made at the respective switching field of each device for reasons

stated previously. As seen in Fig. 4.4, the Co-rich device displays an approximately linear behavior (in a logarithmic scale) with write voltage as predicted by theory outlined in section 2.4 (see equation 2.9). However, the Fe-rich device deviates from this dependence for high voltages where the low probability tail begins to lift. Although the results of only two devices are presented in this chapter, they are representative of a general trend seen across many devices of the two aforementioned compositions. Deviations from expected WER behavior were seen in Fe-rich devices for both switching polarities with varying degrees of magnitude. However, no such deviations were seen in any of the Co-rich devices measured. This so-called anomalous WER has been observed previously [30–34], but the origin of this phenomenon remains speculative and for the most part unknown. Unfortunately, the precise composition of the free layer is not stated in most of the literature where the anomalous WER is observed and therefore the results this work describes cannot be directly compared to prior research in the field.

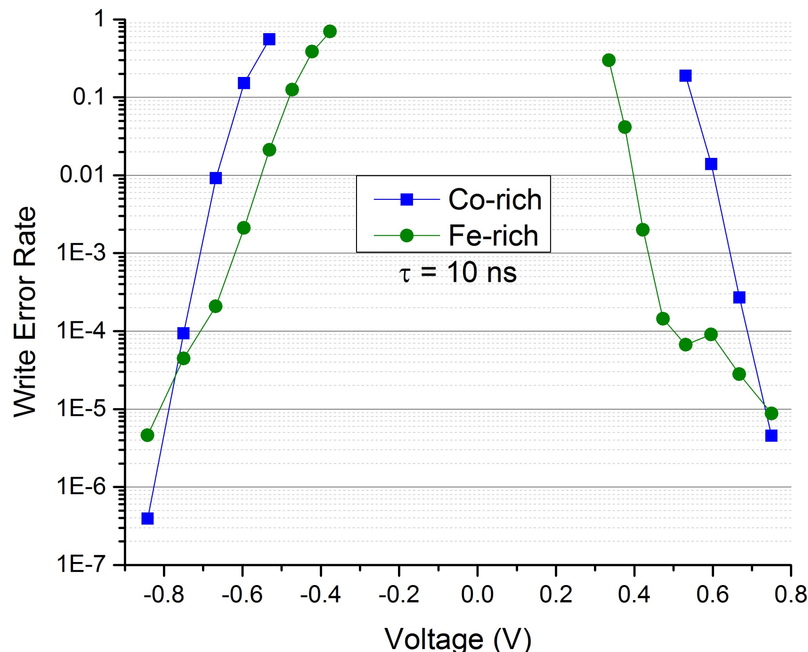

Figure 4.4: Fe-rich and Co-rich WER versus applied write Voltage pulse of 10 ns for both switching polarities. Note the logarithmic scale.

To better understand this anomalous behavior, WER measurements were performed on the Fe-rich device in the same configuration as mentioned previously but for different applied easy-axis fields, seen in Fig 4.5. By changing the applied easy-axis field, one effectively reduces the energy barrier for one polarity of switching. For instance, if the applied field is closer to one side of the hysteresis loop than the other (say 70 Oe for the Fe-rich device in Fig. 4.2), then that side's magnetic state (AP for Fe-rich device) is preferred. Therefore, switching into that state will be easier and switching out of that state will be harder. In Fig. 4.5 there is a clear field dependence of the WER, so much so that the expected exponential dependence returns for switching polarites where the applied field values prefer the final state of the switching attempt. By making the final state energetically more favorable, the anomalous behavior is suppressed. This would suggest one of the proposed possible origins of the anomalous WER in which the magnetization gets "caught" in a meta-stable state of intermediate resistance (between P and AP state resistances) before returning to its initial state during an unsuccessful switching attempt [33] in the high voltage regime where the anomalous behavior occurs. In this scenario, the applied field makes the final state more favorable and therefore eliminates the possibility of entering the meta-stable state responsible for anomalous WERs.

Another related possible origin of the WER anomaly proposed in previous work has to do with sub-volume excitations of the free layer magnetization and other deviations from the macrospin model [34, 35]. To investigate these possible contributions to the anomalous WER, FM ST-FMR spectra were taken on both the Co-rich and Fe-rich devices shown previously to better understand their magnetic dynamics. FM ST-FMR rectified voltage V was measured while sweeping the applied RF frequency for different easy-axis applied fields. Spectra for both P and AP states of the Fe-rich device shown in Fig. 4.6 reveal three distinct modes (resonance peaks), the first of which (lowest frequency) being much larger than the other two (most likely the macrospin predicted quasi-uniform mode). The spectra for P and AP states of the Co-rich device in Fig. 4.7 also show three modes, but with poorer SNR

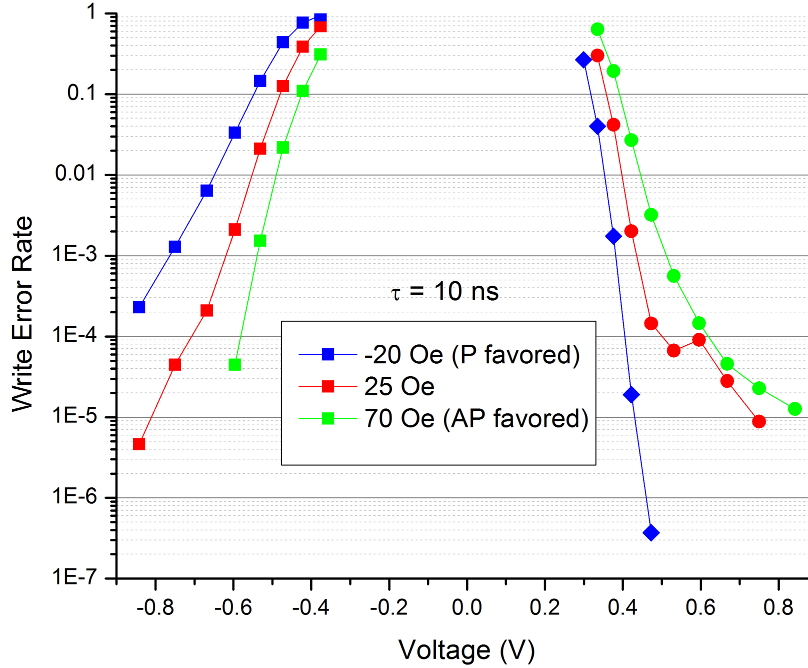

Figure 4.5: Fe-rich WER for different applied fields

most likely due to the Co-rich device having a lower TMR ratio. A higher RF power of -2 dBm was applied to the Co-rich device to account for the diminished signal from poorer TMR, while -10 dBm was applied to the Fe-rich device. The appearance of multiple modes clearly indicates both devices do not behave according to the macrospin model alone as other contributions to the dynamics are visible. Previous correlations have been made between the anomalous WER and ST-FMR measurements indicating energy being sunk into higher order modes at large voltage biases [34]. Possible mechanisms for this energy loss require a frequency coincidence condition where there exists a mode at twice the frequency of the main mode near the switching field, namely parametric resonance excitation [36] and three-magnon scattering [37]. It should be noted that this frequency condition is roughly met for the Fe-rich device (peaks at $\sim$ 2 & 4 GHz) but not for the Co-rich device (peaks near 6, 8, & 10 GHz). This suggests that the Fe-rich device's non-exponential WER for large voltages could be rooted in the energy of the spin current being sunk into higher order spin-wave

modes that are not as effective in reversing the free layer magnetization.

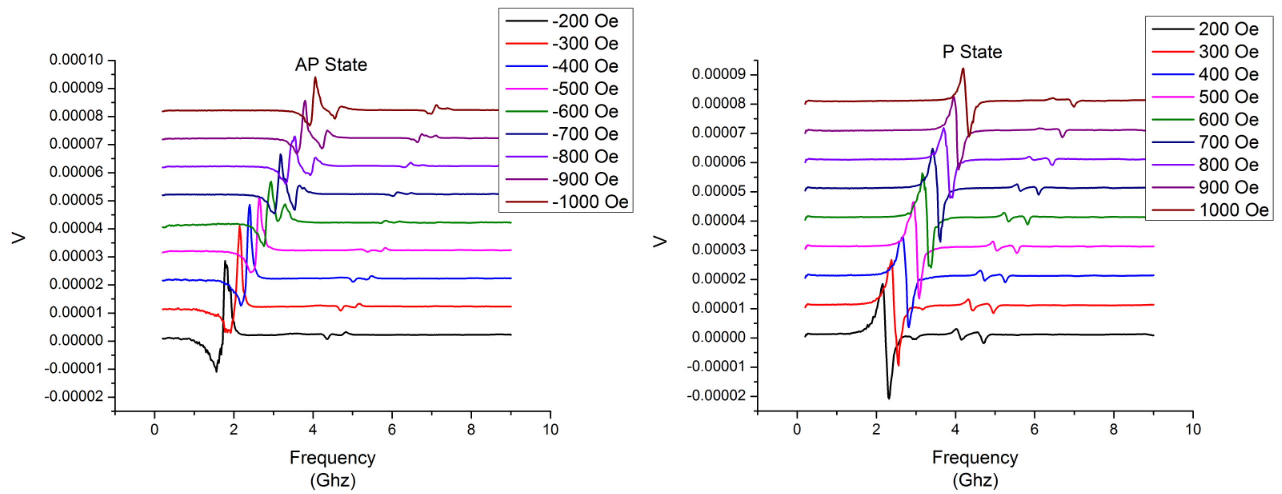

Figure 4.6: Fe-rich ST-FMR spectra for different applied easy-axis fields, vertically offset for clarity

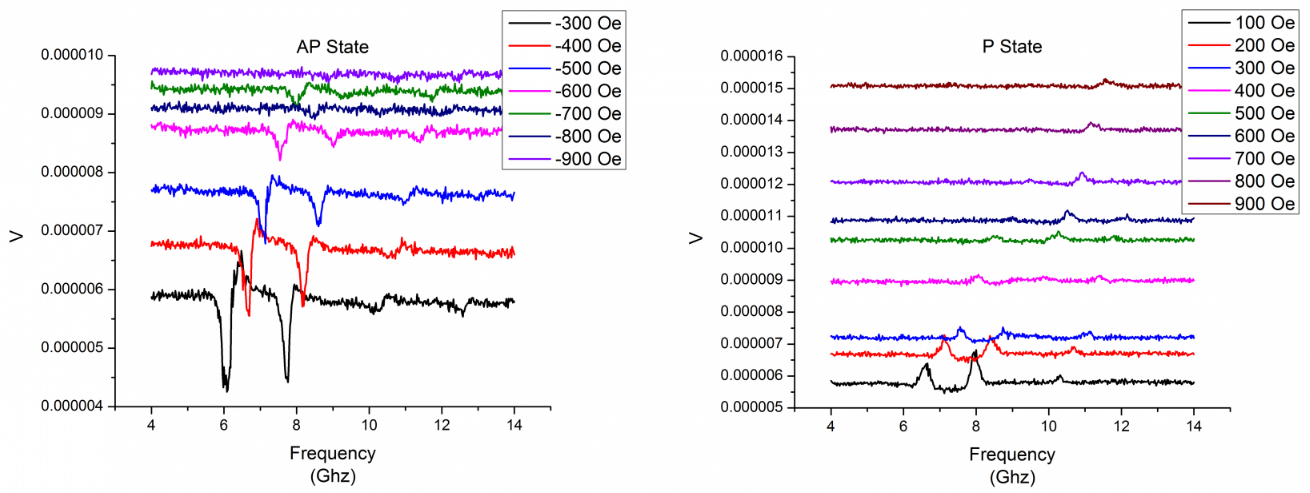

Figure 4.7: Co-rich ST-FMR spectra for different applied easy-axis fields, vertically offset for clarity

Chapter 5

Conclusions

This thesis has addressed two experimental methods for characterizing MTJs for their operational function in STT-MRAM, as well as contextualize these methods with an explanation of the theoretical background on which they're based. These techniques revealed an anomalous behavior of the WER for MTJs with Fe-rich in-plane CoFeB free layers. FM ST-FMR analysis of these anomalous devices identified possible origins of their behavior having to do with non-macrospin dynamics such as precessional energy dissipating into higher order modes. More research is needed into origin of the non-exponential WER to better optimize MTJs for their use as computer memory. If the current pace of improvement and commercialization continues, STT-MRAM will surpass current market-standard memory technologies in the not too distant future.

Bibliography

[1] Y. Huai, "Spin-transfer torque mram (stt-mram): Challenges and prospects," *AAPPS Bulletin*, vol. 18, no. 6, pp. 33–40, 2008.

[2] M. Jullière, "Tunneling between ferromagnetic films," *Physics Letters A*, vol. 54, no. 3, pp. 225–226, 1975.

[3] W. H. Butler et al., "Spin-dependent tunneling conductance of Fe|MgO|Fe sandwiches," *Phys. Rev. B*, vol. 63, p. 054416, 2001.

[4] S. Ikeda et al., "Tunnel magnetoresistance of 604% at 300k by suppression of ta diffusion in cofeb/mgo/cofeb pseudo-spin-valves annealed at high temperature," *Appl. Phys. Lett.*, vol. 93, p. 082508, 2008.

[5] J. Slonczewski, "Conductance and exchange coupling of two ferromagnets separated by a tunneling barrier," *Physical Review B*, vol. 39, no. 10, pp. 6995–7001, 1989.

[6] Jimmy Kan, *ENGINEERING OF METALLIC MULTILAYERS AND SPIN TRANSFER TORQUE DEVICES*. PhD thesis, University of California, San Diego, 2014.

[7] J. Slonczewski, "Current-driven excitation of magnetic multilayers," *Journal of Magnetism and Magnetic Materials*, vol. 159, pp. L1–L7, 1996.

[8] L. Berger et al., "Emission of spin waves by a magnetic multilayer traversed by a current," *Physical Review B*, vol. 54, pp. 9353–9358, 1996.

[9] Chen Wang, *CHARACTERIZATION OF SPIN TRANSFER TORQUE AND MAGNETIZATION MANIPULATION IN MAGNETIC NANOSTRUCTURES*. PhD thesis, Cornell University, 2012.

[10] J. A. Katine and E. E. Fullerton, "Device implications of spin transfer torques," *J. Magn. Magn. Mater*, vol. 320, p. 12171226, 2008.

[11] D. Ralph and M. Stiles, "Spin transfer torques," *Journal of Magnetism and Magnetic Materials*, vol. 320, no. 7, pp. 1190–1216, 2008.

[12] C. Kittel, *Introduction to Solid State Physics*. John Wiley, 1996.

[13] K. Lee et al., "Write error rate slopes of in-plane magnetic tunnel junctions," *Magnetics Letters, IEEE*, vol. 3, p. 3000604, 2012.

[14] L. Néel, “Thorie du tranage magntique des ferromagntiques en grains fins avec application aux terres cuites,” *Geophys.*, vol. 5, p. 99, 1949.

[15] W. F. Brown, “Thermal fluctuations of a singe-domain particle,” *Phys Rev.*, vol. 130, p. 1677, 1963.

[16] W. Wernsdorfer et al., “Experimental evidence of the nel-brown model of magnetization reversal,” *Phys. Rev. Lett.*, vol. 78, pp. 1791–1794, 1997.

[17] Z. Li and S. Zhang, “Thermally assisted magnetization reversal in the presence of a spin-transfer torque,” *Phys. Rev. B*, vol. 69, p. 134416, 2004.

[18] A. Tulapurkar et al., “Spin-torque diode effect in magnetic tunnel junction,” *Nature*, vol. 438, pp. 339–342, 2005.

[19] J. C. Sankey et al., “Spin-Transfer-Driven Ferromagnetic Resonance of Individual Nanomagnets,” *Phys. Rev. Lett.*, vol. 96, p. 227601, 2006.

[20] C. Wang et al., “Bias and angular dependence of spin-transfer torque in magnetic tunnel junctions,” *Phys. Rev. B*, vol. 79, p. 224416, 2009.

[21] G. D. Fuchs et al., “Spin-torque ferromagnetic resonance measurements of damping in nanomagnets,” *Appl. Phys. Lett.*, vol. 91, p. 062507, 2007.

[22] J. C. Sankey et al., “Measurement of the spin-transfer-torque vector in magnetic tunnel junctions,” *Nat. Phys.*, vol. 4, pp. 67–71, 2008.

[23] Xiaoyong Liu et al., “Ferromagnetic resonance and damping properties of CoFeB thin films as free layers in MgO-based magnetic tunnel junctions,” *J. Appl. Phys.*, vol. 110, p. 033910, 2011.

[24] W. S. et al., “Influence of mgo tunnel barrier thickness on spin-transfer ferromagnetic resonance and torque in magnetic tunnel junctions,” *Phys. Rev. B*, vol. 87, p. 094419, 2013.

[25] A. M. Goncalves et al., “Spin torque ferromagnetic resonance with magnetic field modulation,” *Appl. Phys. Lett.*, vol. 103, p. 172406, 2013.

[26] Hitoshi Kubota et al., “Quantitative measurement of voltage dependence of spin-transfer torque in MgO-based magnetic tunnel junctions,” *Nat. Phys.*, vol. 4, pp. 37–41, 2008.

[27] C. Kittel, “On the theory of ferromagnetic resonance absorption,” *Physical Review*, vol. 73, no. 2, pp. 155–161, 1948.

[28] J. Lindner et al., “Two-magnon damping in thin films in case of canted magnetization: Theory versus experiment,” *Phys. Rev. B*, vol. 80, p. 224421, 2009.

[29] R. Heindl et al., “Validity of the thermal activation model for spin-transfer torque switching in magnetic tunnel junctions,” *J. Appl. Phys.*, vol. 109, p. 073910, 2011.

[30] T. Min et al., "A study of write margin of spin torque transfer magnetic random access memory technology," *Magnetics, IEEE Transactions on*, vol. 46, pp. 2322–2327, June 2010.

[31] J. Z. Sun et al., "High-bias backhopping in nanosecond time-domain spin-torque switches of mgo-based magnetic tunnel junctions," *J. Appl. Phys.*, vol. 105, p. 07D109, 2009.

[32] T. Min et al., "Back-hopping after spin torque transfer induced magnetization switching in magnetic tunneling junction cells," *J. Appl. Phys.*, vol. 105, p. 07D126, 2009.

[33] Z. Wang et al., "Bit error rate investigation of spin-transfer-switched magnetic tunnel junctions," *Appl. Phys. Lett.*, vol. 101, p. 142406, 2012.

[34] E. R. Evarts et al., "Correlation of anomalous write error rates and ferromagnetic resonance spectrum in spin-transfer-torque-magnetic-random-access-memory devices containing in-plane free layers," *Appl. Phys. Lett.*, vol. 104, p. 212402, 2014.

[35] J. Z. Sun et al., "Effect of subvolume excitation and spin-torque efficiency on magnetic switching," *Phys. Rev. B*, vol. 84, p. 064413, 2011.

[36] C. Wang et al., "Current-driven parametric resonance in magnetic multilayers," *J. Phys. D: Appl. Phys.*, vol. 46, p. 285001, 2013.

[37] C. Ordez-Romero et al., "Three-magnon splitting and confluence processes for spin-wave excitations in yttrium iron garnet films: Wave vector selective brillouin light scattering measurements and analysis," *Phys. Rev. B*, vol. 79, p. 144428, 2009.

Appendix

A Write Error Rate Code

This is the script used to analyze the WER raw data described in 3.2.

WER.py

```
#This script reads a given raw WER data file (which is two columns of
#voltages before and after each write pulse), converts them to resistances,
#compares the before and after resistances and categorizes each switching
#attempt into three bins: switched (starts in the correct state and ends
#in the opposite state), not switched (starts in the correct state and
#ends in the same state), and missed (states in the incorrect state i.e.
#did not properly reset). These values are summed over all switching
#events in the file and then printed.

import numpy as np
import sys
import scipy as sp
import scipy.optimize

refR =  15000.0 #value of reference resistor in ohms
readV = 0.03 #Applied DC bias in volts
initial = {};
final = {};
switchedSum = 0.0
notswitchedSum = 0.0
missedSum = 0.0

if len(sys.argv) != 2:
    print "Usage: WER.py <path>"
    exit()
```

```
filename = sys.argv[1]

#defines cutoff values for P and AP state resistances for a given
#switching polarity
if "PtoAP" in filename:
    #P to AP
    midReset = 1500
    midWrite = 1500
else:
    #AP to P
    midReset = 1500
    midWrite = 1500

#open raw data file
fin = open(filename, "r")

#Gets rid of headers
for i in range(1,12):
    line = fin.readline()

#calculates resistance from voltage
def res(voltage):
    if (abs(voltage) <=.01*readV):
        return 0.0
    else:
        return refR*abs(voltage)/(abs(readV-voltage))

numLines=0
lcount = 0

#loop to read data file, convert into resistances, and categorize
#switching attempts
while True:
    line = fin.readline()
    if (len(line)==0):
        break
    lcount += 1
    str1,str2 = line.split()
    if (numLines > 0):
        finV = float(str1)
    else:
        str1,str2 = line.split()
        initV = 0.0
        finV = 0.0
```

```
#determines if each before and after resistance is in the correct state
#for a given switching polarity
    if "PtoAP" in filename:
        initial= (res(initV) < midReset)
    else:
        (res(initV) > midReset)# True Low, False High
    if "PtoAP" in filename:
        final  = (res(finV) > midWrite)
    else:
        (res(finV) < midWrite)# True High, False Low

#optional section to print out voltage and calculated resistance for
#a given segment of the data
    if lcount < 2200 and lcount > 2000:
        print numLines,": PR",res(initV),"PW",res(finV), 'V:',initV,finV
    if lcount > 2200:
        break

#catergorizes each event into either missed, switched, or notswitched
#(see beginning of script for definitions of each possibility) and
#sum over all events
    missed = ( res(initV)== 0 or res(finV)==0 or (not initial))
    switched = ((final) and (initial) and (not missed))
    notswitched = ( not (missed or switched))
    if missed:
        missedSum += 1.0
    elif switched:
        switchedSum += 1.0
    elif notswitched:
        notswitchedSum += 1.0
    initV = float(str2)
    numLines+=1

#outputs number of events, number of each switching category,
#switching probability, WER, and checksums
print numLines,"Events Total (File)"
print switchedSum,"Switches"
print notswitchedSum, "No Switches"
print missedSum,"Missed Events | Missed Prob:",missedSum/numLines
print switchedSum+missedSum+notswitchedSum,"Events Total (Calc)"
print "Probability:",switchedSum/(numLines-missedSum)
print "Write Error Rate:",notswitchedSum/(numLines-missedSum)
print "Total:",(switchedSum+notswitchedSum)/(numLines-missedSum)
fin.close()
```

B Phase Adjustment Code

This is the phase optimization code described in 3.1. Essentially, the script takes in the X, Y, and Mag components of the ST-FMR data, minimizes the X channel signal such that the Y channel is maximized with respect to phase angle, and then outputted into a new file with just the frequency and maximized channel signal. The code can also be used for manual manipulation of the phase angle with the help of a basic GUI to be able to see if the signal is appropriately maximized/minimized. This script was originally written by Dr. Igor Barsukov, a Post-Doc also in the research lab of Dr. Krivorotov. This work would like to extend its thanks to Dr. Barsukov for the aid this script provided in data analysis as well as a helpful example in this thesis.

change-phase.py

```
#You have collected measurement data from Lock-In and stored them in
#txt files. The program will read all txt files from the current directory
#and extract the 1st, 2nd, and 3rd columns. It will artificially adjust
#the Lock-In phase the way that X-channel's signal is minimized and thus
#Y-channels signal is maximized. If the automatic phase adjustment does
#not work, you can enter the phase in deg manually. The top subplot of
#the figure displays the original X- and Y- channels. The middle and the
#bottom ones display X- and Y-channels after adjustment, respectively.

import numpy as np
import scipy as sp
import os
import matplotlib.pyplot as plt
from scipy.optimize import minimize
from scipy.optimize import curve_fit
import glob
import thread


''' Global constants '''
PI=Pi=pi=sp.pi
hbar=1.054571726e-34
ubohr=9.27400968e-24
u0=4.0*Pi*1e-7
''' Global contructed constants'''
g2gamma=ubohr/hbar
deg2rad=2*Pi/360.0
rad2deg=360/(2.0*Pi)
''' '''

def trysay(string):
```

```
    try:
        speech.say(string)
    except:
        print string

def lin(x,a,b):
    return a+b*x

def R_fit(angle,data):
    data_alpha=[]
    data_alpha[:] = np.cos(angle*deg2rad)*data[1,:]
                               +np.sin(angle*deg2rad)*data[2,:]
    popt, pcov = curve_fit(lin,data[0],data_alpha,p0=[0,0])
    return 1-(pcov[0,1]/(pcov[0,0]*pcov[1,1]))**2

def find_alpha(alpha,data):
    print
    y=minimize(R_fit,alpha,args=(data,),method='L-BFGS-B',bounds=((0,180),))
    print 'The Lock-In phase has been calculated.'
    print 'alpha= ', y.x[0]
    if not y.success:
        print 'Phase might be OK.'
        thread.start_new_thread( trysay, ("Check the phase!",) )
    return y.x[0]

''' MAIN '''
plt.ion()
alpha=0
newpath='phase-corrected_data'
if not os.path.isdir(newpath):
    os.makedirs(newpath)

for file in glob.glob(os.path.join(os.curdir, '*.txt')):
    print file
    data=np.loadtxt(file,skiprows=8,unpack=True,usecols = (0,1,2))

    try:
        alpha=find_alpha(alpha,data)
    except:
        thread.start_new_thread( trysay, ("Please adjust manually.",) )

    while True:
        data_new=[]
        data_new[:]=-np.sin(alpha*deg2rad)*data[1,:]
                    +np.cos(alpha*deg2rad)*data[2,:]
```

```
        data_zero=[]
        data_zero[:]= np.cos(alpha*deg2rad)*data[1,:]
                     +np.sin(alpha*deg2rad)*data[2,:]

            fig = plt.figure(1)
            subp1 = fig.add_subplot(311)
            subp2 = fig.add_subplot(312)
            subp3 = fig.add_subplot(313)

            subp1.plot(data[0],data[1],'b-', data[0],data[2],'r-')
            subp2.plot(data[0],data_zero,'b-')
            subp3.plot(data[0],data_new,'r-')
            plt.show()

            manual_input=raw_input('Phase in deg or ENTER if phase OK: ')
            plt.clf()
            if not manual_input:
                break
            alpha=float(manual_input)

        writefile = open(newpath+'/'+file,'w')
        np.savetxt(writefile,np.transpose([data[0], data_new]))
        writefile.close()

trysay("Files written. Bye bye.")
''' END MAIN '''
```